Monthly Notices of the ROYAL ASTRONOMICAL SOCIETY

MNRAS **546,** 1–7 (2026) https://doi.org/10.1093/mnras/staf1998
Advance Access publication 2025 November 13

Upper limits on radio emission from the K2-18 system

Kelvin Wandia [1]★ Chenoa Tremblay [2,3,4] Michael A. Garrett,[1,5] Alex Andersson [6,7] Megan G. Li,[8] Vishal Gajjar,[2,3] Robert J. Beswick,[1] Jack F. Radcliffe,[1,9] Daniel Czech ,[6,7] David R. DeBoer ,[3,6,7] P. B. Demorest ,[10] Wael Farah,[2,3] Ian Heywood[7] and Andrew Siemion [1,2,3,6,7,11]

[1]*Jodrell Bank Centre for Astrophysics, University of Manchester, Manchester, M13 9PL, UK*
[2]*SETI Institute, 339 Bernardo Ave, Suite 200, Mountain View, CA 94043, USA*
[3]*Berkeley SETI Research Center, University of California, Berkeley, CA 94720, USA*
[4]*Department of Physics and Astronomy, University of New Mexico, Albuquerque, NM 87131, USA*
[5]*Leiden Observatory, Leiden University, PO Box 9513, NL-2300 RA Leiden, the Netherlands*
[6]*Breakthrough Listen, Astrophysics, Department of Physics, The University of Oxford, Keble Road, Oxford OX1 3RH, UK*
[7]*Astrophysics, Department of Physics, University of Oxford, Keble Road, Oxford OX1 3RH, UK*
[8]*Department of Earth, Planetary, and Space Sciences, University of California, Los Angeles, CA 90095, USA*
[9]*Department of Physics, University of Pretoria, Lynnwood Road, Hatfield, Pretoria, 0083, South Africa*
[10]*National Radio Astronomy Observatory, PO Box O, Socorro, NM 87801, USA*
[11]*University of Malta, Institute of Space Sciences and Astronomy, Msida, MSD 2080, Malta*

Accepted 2025 November 7. Received 2025 November 7; in original form 2025 April 26

ABSTRACT

Stellar and planetary magnetic fields play a crucial role in the habitability of a planet and the integrity of its atmosphere. The detection of methane and carbon dioxide, along with a tentative identification of the potential biosignature dimethyl sulfide/disulfide, in the atmosphere of K2-18 b, a sub-Neptune orbiting an M dwarf star, presents an intriguing question regarding the stellar magnetic environment and the resistance of the planet's magnetosphere (if it exists) to erosion by magnetic activity from the host. To probe for radio emission from the system, we have conducted observations using the Karl G. Jansky Very Large Array at *S*, *C*, and *X* bands (2–4, 5.5–7.5, and 8–10 GHz, respectively) to search for coherent and incoherent radio emission. We detect no radio emission associated with incoherent emission mechanisms. We report 3σ Stokes I upper limits of 49.8 μJy beam^{-1} at *S* band, 17.7 μJy beam^{-1} at *C* band, and 18.0 μJy beam^{-1} at *X* band and an upper limit of the ratio of the radio to the total bolometric luminosity of $\log L_{\rm R}/\log L_{\rm bol} < -8.8$. We have also searched for short duration bursts associated with coherent emission mechanisms at *C* and *X* bands. No signals above a 3σ significance threshold are detected. Although no signals are detected, our radio observations offer constraints, albeit limited, on the stellar magnetic environment supporting recent X-ray observations indicating that K2-18 is a very faint emitter. Our results also contextualize any planetary transmission spectra by providing constraints on the activity level of the host.

Key words: stars: activity – stars:low-mass – stars: magnetic fields.

1 INTRODUCTION

The solar neighbourhood is dominated by low-mass, low-luminosity stars of spectral type M commonly referred to as M dwarfs. This population has been the focus of comprehensive studies that have reported prevalence rates as high as 70−75 per cent of the total main-sequence stellar population in the solar neighbourhood (T. J. Henry et al. 2006; J. G. Winters et al. 2019). M dwarfs have masses of 0.075−0.61 $M_\odot$ (T. J. Henry & W.-C. Jao 2024) and effective temperatures of 2500−4000 K (M. J. Pecaut & E. E. Mamajek 2013). Due to their prevalence and low masses, M dwarfs are favourable targets for radial velocity surveys for exoplanet detection, as they exhibit larger stellar reflex motions compared to stars of other spectral types. The low luminosity of M dwarfs also places the habitable zone close to the star, resulting in short orbital periods (A. L. Shields, S. Ballard & J. A. Johnson 2016). These factors result in a large observational signature for hosted planets, making them well suited for transmission spectroscopy aimed at characterizing exoplanetary atmospheres (L. Kaltenegger, A. Segura & S. Mohanty 2011; R. Cloutier et al. 2017). The internal structure of M dwarfs transitions at masses of 0.31−0.34 $M_\odot$ (I. Baraffe & G. Chabrier 2018) from a radiative core surrounded by a convective envelope akin to our Sun to a fully convective interior. M dwarfs whose mass falls above the transition limit are believed to generate and sustain magnetic fields through an $\alpha\Omega$ dynamo (E. N. Parker 1955) and for those below the limit, the exact mechanism remains uncertain although an α^2 dynamo has been proposed (G. Chabrier & M. Küker 2006; W. Dobler, M. Stix & A. Brandenburg 2006; M. K. Browning 2008). These dynamos are driven by stellar rotation and convection (P. Charbonneau 2010; A. Reiners, M. Schüssler & V. M. Passegger 2014). Although magnetic fields are prevalent in all stars (G. Mathys, S. K. Solanki & D.

★ E-mail: kelvin.wandia@manchester.ac.uk

T. Wickramasinghe 2001; S. V. Berdyugina 2009), M dwarfs exhibit enhanced magnetic fields compared to main-sequence stars of earlier spectral types (D. Shulyak et al. 2019) due to large convective eddies in their deep (or fully) convective zones, which lead to large-scale organized magnetic fields (G. Chabrier & M. Küker 2006).

The strong internal magnetic fields drive significant surface activity in the form of stellar spots, plages, faculae, and flares. This activity results in surface inhomogeneities, which are a potential source of bias for absorption features in transmission spectra (T. Barclay et al. 2021). The magnetic fields also heat the stellar atmosphere leading to chromospheric emission in the optical (e.g. M. N. Günther et al. 2020), ultraviolet (UV; e.g. K. France et al. 2013), and coronal emission in the X-ray (e.g. M. Caramazza et al. 2023) and radio (e.g. J. R. Callingham et al. 2021). At radio wavelengths, particularly at centimetre wavelengths, the dominant process responsible for incoherent emission from M dwarfs is the gyrosynchrotron radiation mechanism. Gyrosynchrotron radiation arises from mildly relativistic electrons in a hot plasma from thermal (the high-energy tail of a Maxwellian distribution; W. W. Golay et al. 2023) or non-thermal energy distributions (G. A. Dulk, D. B. Melrose & S. M. White 1979; G. A. Dulk 1985). The radio emission observed from gyrosynchrotron processes occurs at harmonics s (typically$10 \lesssim s \lesssim 100$) of the local cyclotron frequency ν_c (MHz) $= 2.8 \times$ B (G) (M. Güdel 2002). Another process that occasionally contributes to incoherent emission is synchrotron radiation from highly relativistic electrons in a non-thermal energy distribution. For detected incoherent radio emission, the mechanism responsible can be determined using the degree of circular polarization commonly quantified through measurements of the Stokes V parameter. Radio emission from gyrosynchrotron processes exhibits a moderate degree of circular polarization, while emission from synchrotron processes exhibits negligible circular polarization but is often highly linearly polarized. Finally, we note that the inverse Compton catastrophe limits the brightness temperatures of incoherent mechanisms to $\lesssim 10^{12}$ K (K. I. Kellermann & I. I. K. Pauliny-Toth 1969).

In contrast, radio emission with brightness temperatures far in excess of 10^{12} K have been detected from stars (e.g. J. R. Callingham et al. 2021), which is indicative of coherent emission mechanisms. Such emission has been attributed to plasma emission and electron cyclotron masers. In the former, energetic beams of electrons or other instabilities cause perturbations in the plasma, which excite Langmuir waves at the local plasma frequency $\nu_p \sim 9\sqrt{n_e}$ kHz. The Langmuir waves are then converted to radio waves due to non-linear wave interactions in the plasma (H. A. S. Reid & E. P. Kontar 2017). Plasma emission is observed in the first and second harmonics (D. B. Melrose 1980) and is dominant at frequencies <1 GHz (S. Pohjolainen & N. Talebpour Sheshvan 2020). In contrast, the electron cyclotron maser emission (ECME; C. S. Wu & L. C. Lee 1979) arises due to population inversion caused by electrons trapped in a flux tube leading to magnetic mirroring of electrons with large pitch angles. The distribution of the electrons is uncertain, although loss-cone and horseshoe distributions have been proposed (see D. B. Melrose 2017). The anisotropy in the electron distribution results in maser action with stimulated emission occurring at ν_c (D. B. Melrose 2017).

Radio emission generated by the mechanisms discussed above has been detected from M dwarfs at radio wavelengths. Quiescent emission (e.g. A. J. Burgasser & M. E. Putman 2005; L. N. Driessen et al. 2022; K. Wandia et al. 2025) and flaring emission (e.g. A. Andersson et al. 2022) both attributed to gyrosynchrotron processes have been reported. Similarly, synchrotron radiation has been observed from radiation belts of later spectral type M dwarfs (J. B. Climent et al. 2023; M. M. Kao et al. 2023). Coherent emission attributed to either plasma emission or ECME from the corona and/or originating from large-scale magnetic fields driving auroral emission (e.g. J. Villadsen & G. Hallinan 2019; J. R. Callingham et al. 2021; A. J. Gloudemans et al. 2023; J. S. Pineda & J. Villadsen 2023; O. M. Smirnov et al. 2025) has also been detected. Significant insights can be drawn from these detections, e.g. the magnetic field strengths of the emitting region or object, physical source sizes, geometry of the emitting objects, and electron number densities of the plasma. Radio emission can also be generated by the interaction between the stellar wind and a hosted planet's magnetosphere. This emission arises when the ionized component of the incident stellar wind from the host star impinges on the magnetosphere and magnetic reconnection occurs at the magnetopause. Particles are accelerated along the planet's magnetic field lines and funnelled towards the planet's poles. Magnetic mirroring then reflects back particles with large pitch angles, leading to emission (see J. R. Callingham et al. 2024, and references therein). This mechanism is routinely seen on Earth, especially on the dayside of the magnetosphere. *In situ* measurements of radio power from the magnetospheres of five Solar system planets, Earth and the four gas giants, have led to the formulation of a power scaling relation referred to as the radiometric Bode's law (RBL), which is useful in estimating the flux densities of extra-solar systems (W. M. Farrell, M. D. Desch & P. Zarka 1999; P. Zarka et al. 2001; W. Lazio et al. 2004; E. O'Gorman et al. 2018).

Estimating the magnetic field strengths and understanding the magnetic environment of M dwarfs is both critical for habitability, e.g. planets orbiting highly active M dwarfs may experience significant atmospheric erosion before achieving stability, potentially rendering them uninhabitable (see O. Venot et al. 2016; H. Nicholls et al. 2023), and in disentangling stellar contamination from the true atmospheric signals. Targeted spectroscopic studies of planets orbiting nearby M dwarfs have revealed a new class of temperate ocean worlds called 'Hycean Worlds' (N. Madhusudhan, A. A. A. Piette & S. Constantinou 2021). In particular, potential biosignatures, carbon dioxide and methane (N. Madhusudhan et al. 2023), have been detected in the atmosphere of one of these exoplanets, K2-18 b, using the *James Webb Space Telescope*. A tentative detection of the abiotic biosignatures dimethyl sulfide and dimethyl disulfide has also been recently claimed by N. Madhusudhan et al. (2025). The claimed detection of biosignatures from K2-18 b makes the host star an interesting candidate to probe for radio emission. In this manuscript, we describe the K2-18 system in Section 2. In Section 3, we discuss the Very Large Array (VLA) observations and data analysis. In Section 4, we discuss some mechanisms through which radio emission is generated. Finally, we present our conclusions in Section 5.

2 THE K2-18 SYSTEM

The K2-18 system consists of a 2.4 ± 0.6 Gyr old (E. F. Guinan & S. G. Engle 2019) M dwarf star of spectral type M2.5 (A. Schweitzer et al. 2019) at a distance of ∼38.1 pc from the Earth (L. Lindegren et al. 2021) and hosts two exoplanets, K2-18 b (B. T. Montet et al. 2015) and K2-18 c (R. Cloutier et al. 2017). K2-18 b is a sub-Neptune orbiting at a distance of ∼0.14 au from the star with an orbital period of ∼33 d (P. Sarkis et al. 2018) and is hypothesized to be either tidally locked or in a state of spin–orbit resonance (B. Charnay et al. 2021). The physical parameters of the star and planet are listed in Table 1. Recent analysis of *XMM–Newton* observations places the soft X-ray (0.2–2.0 keV) flux at $F_X \sim 5.89 \times 10^{-15}$ erg cm^{-2} s^{-1} corresponding to an X-ray luminosity of $L_X \sim 27.0$ erg s^{-1} consistent with a very

Table 1. Physical parameters of the K2-18 system. References: (1) A. Schweitzer et al. (2019), (2) L. Lindegren et al. (2021), (3) P. Sarkis et al. (2018), (4) B. Benneke et al. (2019), (5) E. F. Guinan & S. G. Engle (2019), and (6) S. Rukdee et al. (2025).

Property	K2-18	K2-18 b	Reference
SpT	M2.5	–	1
Distance (pc)	38.1	38.1	2
Mass ($M_\odot$, M_J)	0.4951 ± 0.0043	$\sim$0.028	3
Radius ($R_\odot$, R_J)	0.4445 ± 0.0148	0.211 ± 0.20	3
T ($T_{\rm eff}$, $T_{\rm eq}$) (K)	3457 ± 39	254.9 ± 3.9	4
$P_{\rm rot}$ (d)	39.63 ± 0.50	–	4
Orbital period (d)	–	$\sim$32.94	4
Orbital distance (au)	–	$\sim$0.143	4
Age (Gyr)	2.4 ± 0.6	–	5
$F_{\rm X}$ (erg cm^{-2} s^{-1})	5.89×10^{-15}	–	6

faint emitter. This inactivity is consistent with the findings of A. Modi, R. Estrela & A. Valio (2023) who reveal that the planet has retained its atmosphere despite erosion from extreme UV irradiation. These conclusions are strengthened by earlier investigations on the escape rate of the planet's atmosphere by L. A. dos Santos et al. (2020) who demonstrated that the planet will lose <1 per cent of its mass over its lifetime. We note that the low quiescent X-ray flux of the system does not preclude the occurrence of sporadic large flares and the presence of magnetic phenomena detectable at radio wavelengths.

3 RADIO DATA

3.1 Observations

We observed the K2-18 system using the VLA, which consists of 27 antennas arranged into 3 arms, each with 9 antennas, to form a Y shape. The observations were conducted over $\sim$12 weeks from 2023 September 29 to 2023 December 21 sparsely sampling the planet's orbit as a part of a technosignature search (C. D. Tremblay et al., in preparation) utilizing the Commensal Open-Source Multimode Interferometer Cluster (C. D. Tremblay et al. 2024) and the standard `WIDAR` back end.

The bulk of the observations were conducted at *S* band (2–4 GHz) over two sessions separated by 9 d. The first observation used the VLA in a non-standard hybrid configuration as the array was being reconfigured from the A to D (A→D) configuration resulting in seven antennas in the A configuration and the rest in the D configuration. The second observation was conducted using the standard D configuration. In the hybrid configuration, the resultant A-configuration maximum baseline length in wavelength λ at *S* band is $406\,k\lambda$, a factor of $\sim$40 larger than the corresponding longest baseline of the D configuration. The baseline mismatch leads to a pronounced change in the uv- coverage that is not reflected in the integration time resulting in a significantly distorted point spread function (PSF).

The observation set-up included a polarization leakage calibrator J1407+2827, which was observed at the start of each observation. The phase, bandpass, and amplitude calibrator J1120+1420 was interleaved with observations of the target K2-18. Finally, 3C286, a standard VLA flux and polarization angle calibrator, was observed. For each session, the target was observed over six scans each $\sim$14-min long yielding an on-target time of $\sim$84 min. The remaining observations were short 10-min (on-source) single scan snapshots using the standard A and D configurations in the *S*, *C* (5.5–7.5 GHz), and *X* (8–10 GHz) bands. Four snapshots were obtained in each of the frequency bands when the array was in the D configuration. When the array had changed to the A configuration, two snapshots were obtained at *S* band and a single snapshot at the *C* and *X* bands. The calibrator set-up was similar to the main data set, except that the polarization leakage calibrator was not observed. All the data were digitized at 8 bits with the correlator in continuum mode. A summary of the observations is listed in Table 2.

We highlight that *S*-band observations using the D configuration of the VLA are affected by source confusion due to the large synthesized beams. This results in blending of multiple faint sources that cannot be resolved individually. The array is then effectively confusion limited with the lower noise bound set by the confusion noise, e.g. the confusion limit is $\sim$12 μJy beam^{-1}[1] for *S*-band D-configuration observations. Confusion in the other configurations and at higher frequencies is negligible. In addition to confusion noise, *S*-band D-configuration observations are significantly impacted by radio frequency interference (RFI).

3.2 Calibration

We processed the data using the VLA Calibration Pipeline 2024.1.0.8,[2] which is integrated into the Common Astronomy Software Applications (CASA; J. P. McMullin et al. 2007; CASA Team et al. 2022, version 6.6.1). The pipeline first imports the data stored in a Science Data Model-Binary Data Format [SDM-BDF] to a measurement set (MS), performs Hanning smoothing to reduce Gibbs ringing, applies online flags, and performs various calibration steps ranging from antenna position corrections to gain and phase calibrations. Automatic flagging of RFI is also executed. Finally, the data are science ready. We note that plots are made at various steps to serve as a diagnostic for the calibration quality. For the two 84-min *S*-band observations, J1407+2827 was used to correct for polarization leakage between the feeds and 3C286 was used to calibrate the absolute position of the polarization angle. Polarization calibration for the snapshot observations was not possible as a polarization leakage calibrator was not available.

3.3 Imaging and self-calibration

To assess the quality of the data calibration, we produced images using the CASA task `tclean`. We employed the Multi-Term Multi-Frequency Synthesis (U. Rau & T. J. Cornwell 2011) deconvolver to account for the large observing bandwidth (2 GHz). The images were also Briggs weighted (D. S. Briggs 1995) with a robust parameter of 0.5 (biasing slightly towards natural weighting). We observed no distinct emission at the position of the K2-18 system. In the images, the noise significantly deviated from the expected noise floor set by the confusion limit for *S*-band D-configuration observations and the thermal noise for the rest of the observations. Upon closer examination, the cause of the elevated noise was determined to be QSO B1127+078, a bright quasar located $\sim$3 arcmin from the target position (L. Petrov & Y. Kovalev 2025) at a peak flux density in the D configuration of $\sim$50, $\sim$22, and $\sim$10 mJy beam^{-1} at *S*, *C*, and *X* bands, respectively. Imaging artefacts associated with the quasar significantly limited the dynamic range of the images.

[1] VLA Exposure Calculator
[2] VLA Calibration Pipeline 2024.1.0.8

Table 2. List of observation of K2-18 ordered by date. The bands are defined by their designated frequency ranges, the *S* band covers 2–4 GHz, *C* band covers 5.5–7.5 GHz, and *X* band covers 8–10 GHz. The observations were conducted using the A and D configurations of the VLA. The bulk of the data were observed at *S* band over two epochs, each lasting 84 minutes. The rest of the observations were short 10-min scans. The restoring beam for each observation obtained from self-calibrated images is also presented. The details of the self-calibration parameters are presented with p denoting phase-only self-calibration and ap denoting amplitude-and-phase self-calibration. The solution intervals are also reported, where inf corresponds to the full scan length and int corresponds to the integration time. The integer preceding p or ap specifies the self-calibration rounds with the last iteration indicating convergence.

Obs. date	Band	Configuration	Time on source (min)	Restoring beam (arcsec × arcsec)	Self-calibration parameters	1σ rms (μJy beam^{-1})	
						Stokes I	Stokes V
29/09/2023	*C*	A	10	1.0 × 0.3	5 p only (inf, 148 s, 36 s, 8 s, int) and 1 ap (inf)	14.0	12.2
29/09/2023	*X*	A	10	0.5 × 0.2	5 p only (inf, 148 s, 36 s, 8 s, int)	11.5	9.8
30/09/2023	*S*	A	10	1.3 × 0.6	5 p only (inf, 148 s, 36 s, 8 s, int)	16.6	13.3
30/09/2023	*S*	A	10	1.0 × 0.6	4 p only (inf, 148 s, 36 s, 8 s)	15.0	11.5
13/10/2023	*S*	A→D	84	6.5 × 1.3	–	71.3	16.0[a]
22/10/2023	*S*	D	84	19.2 × 17.3	2 p only (inf, 166 s) and 1 ap (inf)	29.0	9.7
01/12/2023	*S*	D	10	22.4 × 19.1	4 p only (inf, 148 s, 36 s, 8 s) and 1 ap (inf)	30.1	22.5
01/12/2023	*C*	D	10	18.2 × 8.9	3 p only (inf, 148 s, 36 s) and 1 ap (inf)	16.5	12.2
01/12/2023	*X*	D	10	16.8 × 6.2	1 p only (inf)	44.8	35.5
08/12/2023	*S*	D	10	36.0 × 19.0	5 p only (inf, 148 s, 36 s, 8 s, int) and 1 ap (inf)	51.9	21.9
08/12/2023	*C*	D	10	15.2 × 9.2	3 p only (inf, 148 s, 36 s) and 1 ap (inf)	14.1	10.3
08/12/2023	*X*	D	10	10.8 × 6.8	1 p only (inf)	13.6	9.0
13/12/2023	*X*	D	10	11.3 × 6.6	3 p only (inf, 148 s, 36 s) and 1 ap (inf)	13.4	10.6
14/12/2023	*S*	D	10	25.1 × 18.5	5 p only (inf, 148 s, 36 s, 8 s, int) and 1 ap (inf)	46.5	14.9
14/12/2023	*C*	D	10	12.6 × 9.4	5 p only (inf, 148 s, 36 s, 8 s, int) and 1 ap (inf)	14.3	10.2
18/12/2023	*X*	D	10	12.3 × 6.7	3 p only (inf, 148 s, 36 s) and 1 ap (inf)	11.2	9.3
19/12/2023	*C*	D	10	13.3 × 9.3	2 p only (inf, 148 s) and 1 ap (inf)	13.2	9.5
21/12/2023	*S*	D	10	36.5 × 16.9	3 p only (inf, 148 s, 36 s)	70.3	27.3

Note. [a]In an attempt to shape the PSF, a uniformly weighted (robust = −1) Gaussian taper of beamwidth equivalent to the B-configuration VLA resolution at *S* band (∼2.1 arcsec) was applied to the visibilities; nonetheless, self-calibration was unsuccessful.

To improve the fidelity of the images, we performed self-calibration using the official pipeline self-calibration scripts,[3] which we edited to fit our needs. For each band, we produced a wide-field image of size 1.5 times the primary beam at *S* band and covering the entire primary beam at *C* and *X* bands. All the images encompassed the target, the bright quasar, and multiple faint sources in the field of view. We then performed self-calibration for each of the observations using the parameters listed in Table 2. We note that the *S*-band D-configuration data are significantly degraded by RFI and require extensive flagging resulting in noise levels significantly above the confusion limit of ∼12 μJy beam^{-1}. The noise levels for the 10-min snapshots at *C* and *X* bands are consistent with the theoretical thermal noise level of ∼9 μJy beam^{-1} for a dual polarization Stokes I Briggs weighted image. The noise levels for all the observations in the Stokes I and V are listed in Table 2. Attempts at self-calibration were unsuccessful for the data observed using the hybrid configuration due to the poorly characterized PSF. Excluding the seven antennas in the A configuration did not mitigate the issue, as the data were extensively flagged leaving only a small (<5 per cent) unusable subset. Similarly, tapering the UV coverage and changing the weighting scheme did not alleviate the problem. Consequently, the data were excluded from further analysis.

3.4 Variability analysis

To search for short duration bursts, we began by subtracting the CLEAN components stored in the `modelcolumn` of the MS from the self-calibrated visibilities using the CASA task `uvsub`. Since the target was not detected, it was not included in the self-calibration mask and thus not deconvolved. Consequently, the `modelcolumn` contained no associated CLEAN components precluding any risk of subtraction. To subtract faint μJy sources that were otherwise not included in the self-calibration model, we generated large images similar in size to those discussed in the preceding section, masked the target position, deconvolved the images in the Stokes I and V using `WSClean` (A. R. Offringa et al. 2014), and similarly subtracted the CLEAN components from the visibilities using `uvsub`. We then used the `table` and `ms` tools available via the CASATOOLS package to parse the MS after which we averaged all baselines, frequency channels, and spectral windows and binned the data at a cadence of 1 min yielding a single visibility per bin. Subsequently, we produced light curves for the *C*- and *X*-band observations. Light curves for the *S*-band observations were not produced due to extensive flagging of the data in addition to difficulties in accurately subtracting the numerous faint background sources.

[3]https://github.com/jjtobin/auto_selfcal

4 RADIO EMISSION

4.1 Planetary auroral emission

The RBL described in Section 1 is used to determine the median power output caused by the impinging ionized stellar wind on the planet's magnetosphere. The emission is at a central frequency ν_c presented by W. M. Farrell et al. (1999) as

$$\nu_c \sim 23.5 \left(\frac{\omega_P}{\omega_J}\right) \left(\frac{M_P}{M_J}\right)^{5/3} \left(\frac{R_p}{R_J}\right)^3 \text{ MHz}, \quad (1)$$

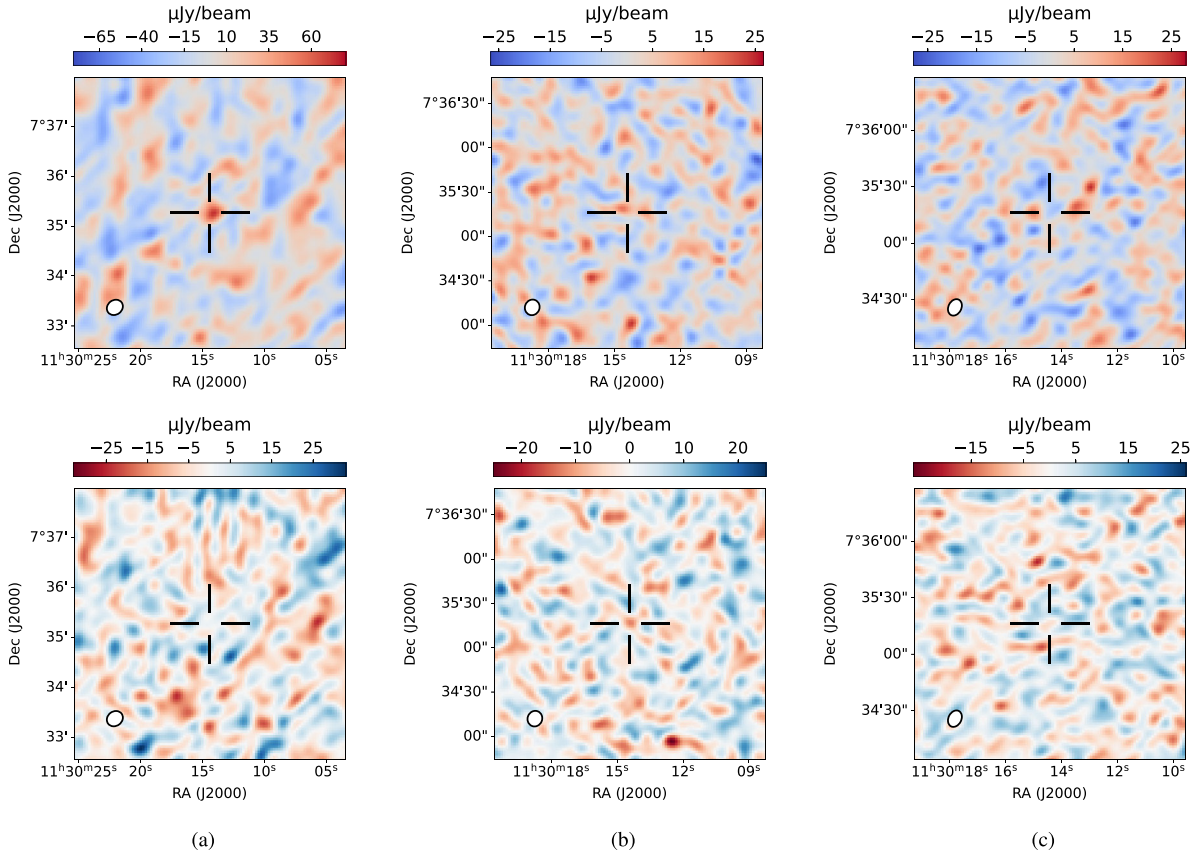

Figure 1. (a) *S*-band Stokes I image (top) and Stokes V (bottom). The Stokes I 1σ rms noise is 16.6 μJy beam^{-1} and the corresponding 1σ rms noise of the Stokes V image is 7.1 μJy beam^{-1}. (b) *C*-band Stokes I image (top) and Stokes V (bottom). The Stokes I 1σ rms noise is 5.9 μJy beam^{-1} and the corresponding 1σ rms noise of the Stokes V image is 5.0 μJy beam^{-1}. (c) *X*-band Stokes I image (top) and Stokes V (bottom). The Stokes I 1σ rms noise is 6.0 μJy beam^{-1} and the corresponding 1σ rms noise of the Stokes V image is 5.2 μJy beam^{-1}. The black cross in the images indicates the position of K2-18. The restoring beam is shown in the filled white circle on the bottom left of each image. All the images are produced from observations conducted using the D configuration of the VLA.

and the median emitted radio power $P_{\rm rad}$ as (W. M. Farrell et al. 1999)

$$P_{\rm rad} = 4 \times 10^{18} \left(\frac{\omega_{\rm P}}{\omega_{\rm J}}\right)^{0.79} \left(\frac{a_{\rm p}}{a_{\rm J}}\right)^{-1.60} \left(\frac{M_{\rm P}}{M_{\rm J}}\right)^{1.33} \ {\rm erg\,s^{-1}}. \quad (2)$$

In equations (1) and (2), ω, a, M, and R are the rotation period, orbital distance, mass, and radius, respectively. The subscripts 'P' and 'J' indicate values for the planet and Jupiter, respectively. Using equation (1), we estimate $\upsilon_{\rm c} \sim 45$ kHz, which is below the plasma frequency (∼10 MHz) of the Earth's ionosphere, and therefore not detectable from ground-based radio observatories. We determine a median radio power output of $P_{\rm rad} \sim 3.2 \times 10^{20}$ erg s^{-1}, and a median flux of $F_\nu \sim 8.2 \times 10^{-26}$ erg s^{-1} cm^{-2} Hz^{-1} or ∼8.2 mJy, using $F_\nu = P_{\rm rad}/4\pi d^2 \Delta\nu$, where $\Delta\nu = 0.5\nu_{\rm c}$ (see W. M. Farrell et al. 1999). We note that we have assumed isotropic beaming in the evaluation of the flux density. Although such fluxes will be accessible to future space observatories, the frequencies of the emission may remain inaccessible due to free–free absorption of the radio waves along the line of sight by the interstellar medium, especially for distant star–exoplanet systems (see B. Burkhart & A. Loeb 2017).

4.2 Coronal gyrosynchrotron emission

Radio emission from the hot corona of K2-18 is likely to occur via gyrosynchrotron processes as is typical for M dwarfs. To search for slowly varying emission arising from gyrosynchrotron processes, we combined data for each observing epoch and band and generated images and made no detection. Using the more sensitive (due to more snapshots) D-configuration observations, we placed 3σ Stokes I and V constraints of 49.8 and 21.3 μJy beam^{-1} at *S* band, 17.7 and 15.0 μJy beam^{-1} at *C* band, and 18.0 and 15.6 μJy beam^{-1} at *X* band. We present the combined images showing the 1σ rms for each observing band in Fig. 1.

To place limits on the luminosities, we first estimate the bolometric luminosity $L_{\rm bol}$ using the Stefan Boltzmann's law, $L_{\rm bol} = 4\pi\sigma_{\rm sb}R^2T_{\rm eff}^4$, where $\sigma_{\rm sb}$ is the Stefan Boltzmann's constant and R and $T_{\rm eff}$ are the radius and effective temperature of K2-18, respectively. We determine $\log L_{\rm bol} \sim 32.0$ erg s^{-1} using the parameters in Table 1. For the spectral luminosity $L_\nu = 4\pi d^2 S_\nu$ where d is the distance to K2-18 and S_ν is the flux density, we estimate $\log L_\nu <$ 14.0 erg s^{-1} Hz^{-1} at *S* band, <13.5 erg s^{-1} Hz^{-1} at *C* band, and <13.5 erg s^{-1} Hz^{-1} at *X* band. The corresponding radio luminosities $L_{\rm R} = \int L_\nu {\rm d}\nu$, where d$\nu$ is the observing bandwidth, are $\log L_{\rm R} <$ 23.2 erg s^{-1} at *S* band, <22.8 erg s^{-1} at *C* band, and <22.8 erg s^{-1} at *X* band and determine a ratio of the radio to bolometric luminosities of $\log L_{\rm R}/\log L_{\rm bol} < -8.8$ for the three observing bands.

Using the X-ray luminosity of $\log L_{\rm X} \sim 27.0$ erg s^{-1} and the measured *C*-band (5 GHz) upper limits on the radio luminosity, we establish that the luminosity is possibly in agreement with the Güdel–Benz relationship, which relates the soft X-ray emission to

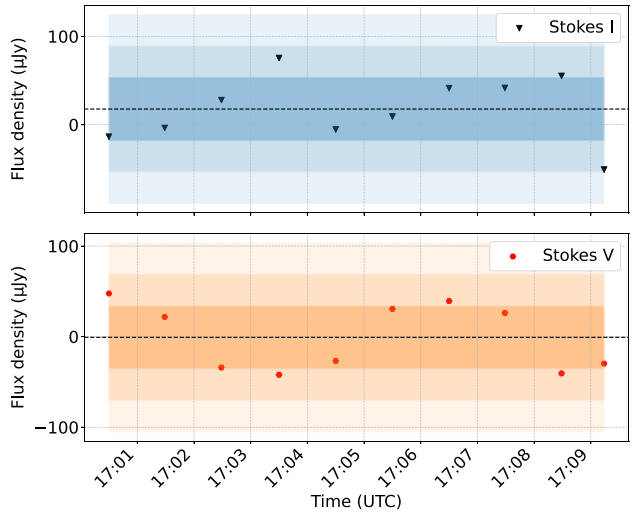

Figure 2. *C*-band light curves of K2-18 for the observation conducted on 2023 December 8 using the VLA in its D configuration. The visibilities are binned at a cadence of 1 min. The broken line represents the mean values in the Stokes I and V at ∼17.6 and ∼−0.8 μJy, respectively. The rms noise σ is ∼35.4 and ∼34.8 μJy in the Stokes I and V and is represented by the shaded region with decreasing intensity corresponding to 1σ, 2σ, and 3σ, respectively.

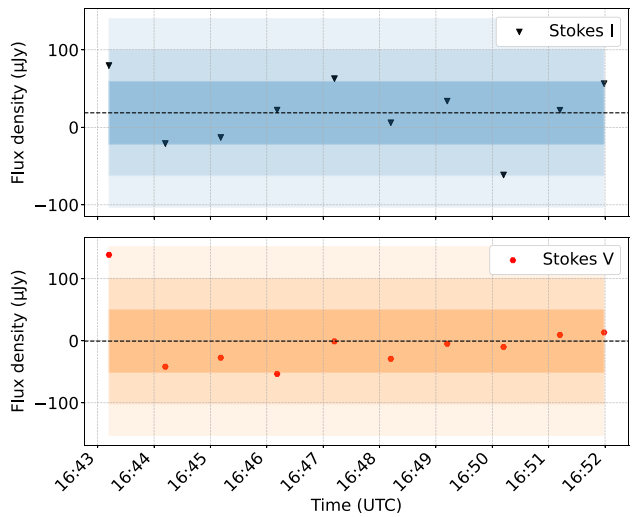

Figure 3. *X*-band light curves of K2-18 for the observation conducted on 2023 December 18 using the VLA in its D configuration. The visibilities are binned at a cadence of 1 min. The broken line represents the mean values in the Stokes I and V at ∼18.7 and ∼−0.6 μJy, respectively. The rms noise σ is ∼40.6 and ∼50.8 μJy in the Stokes I and V and is represented by the shaded region with decreasing intensity corresponding to 1σ, 2σ, and 3σ, respectively.

the 5 GHz radio luminosity as follows: $\log L_X \lesssim \log L_R + 15.5$ (M. Guedel & A. O. Benz 1993).

4.3 Electron cyclotron maser emission

We searched for short duration bursts, which are characteristic of ECME due to coronal or auroral emission by generating light curves from the *C*- and *X*-band observations. We present the light curves in Figs 2 and 3. We did not detect any emission at the location of K2-18 above 3σ, where σ is the rms noise in an observing cadence of 1 min. Given the null detection of K2-18, we present one example per band by selecting the data set with the best self-calibration and lowest noise in the Stokes I and V to demonstrate the absence of a detectable signal.

5 CONCLUSIONS

The *James Webb Space Telescope*, through transmission spectroscopy, has opened a new window into the study of exoplanetary atmospheres. Over its mission lifetime, the telescope is expected to characterize the atmospheres of some of the nearby stars, many of which are M dwarfs. The detection of biosignatures is within sight, and a unified approach involving radio observations is necessary to truly constrain habitability. Radio observations will also prove crucial to constraining the magnetic properties of M dwarfs, by providing direct measurements of magnetic field strengths and potentially activity levels by detecting radio emission associated with magnetic phenomena.

In this manuscript, we have analysed VLA radio observations conducted over 12 weeks at a frequency bandwidth ranging from 2 to 10 GHz and reported null detections for slowly varying emission associated with gyrosynchrotron processes. We have placed 3σ upper limits of 49.8 μJy beam^{-1} at *S* band, 17.7 μJy beam^{-1} at *C* band, and 18 μJy beam^{-1} at *X* band. We similarly place 3σ upper limits for the spectral luminosity at $\log L_\nu < 14.0$ erg s^{-1} Hz^{-1} and a ratio of the radio to bolometric luminosity of $\log L_R / \log L_{bol} < -8.8$, where $\log L_{bol}$ is the total bolometric luminosity at ∼32 erg s^{-1}. We have further searched for short duration bursts from ECME using light curves produced from *C*- and *X*-band observations and made no detection at a 3σ level. These constraints are vital for building realistic models of stellar surface inhomogeneities and mitigating their impact on the interpretation of transmission spectra. In particular, the null detection of incoherent emission associated with gyrosynchrotron emission may imply a low flaring rate for K2-18, translating to lower temporal variability in the transmission spectra and a low filling rate for spots and faculae. These findings are supported by recent analysis of X-ray data from the system by S. Rukdee et al. (2025) and may suggest that planetary transmission spectra from K2-18 b are free from contamination; nevertheless, we advise caution in their interpretation owing to the sparse sampling of the planet's orbit in our observations.

We highlight that there are several factors affecting detectability of radio emission from these mechanisms. The viewing angle of the instrument is particularly important for ECME-driven emission, which requires favourable observing angles. The magnetic field strength also affects the emission frequency for both ECME gyrosynchrotron and physical properties of the plasma; e.g. high number densities lead to suppression of gyrosynchrotron radio emission due to Razin–Tsytovich effect (G. A. Dulk 1985) and similarly very dense plasma inhibits the propagation of radio waves associated with ECME (see M. Güdel 2002). We also establish that radio emission from the planet's magnetosphere is undetectable with current Earth-bound instruments.

ACKNOWLEDGEMENTS

This project has been made possible in part by a grant from the SETI Institute. This work made use of ASTROPY:3, a community-developed core PYTHON package and an ecosystem of tools and resources for astronomy (Astropy Collaboration 2013, 2018, 2022). This research has made use of the NASA Exoplanet Archive, which is operated by the California Institute of Technology, under contract

with the National Aeronautics and Space Administration under the Exoplanet Exploration Program. The National Radio Astronomy Observatory is a facility of the National Science Foundation operated under cooperative agreement by Associated Universities, Inc. We thank the anonymous referee for their useful comments, which have substantially improved the manuscript.

DATA AVAILABILITY

Data underlying this article are publicly available in the National Radio Astronomy Observatory (NRAO) Data Archive at https://data.nrao.edu/portal and can be accessed with project code 23B-307.

REFERENCES

Andersson A. et al., 2022, MNRAS, 513, 3482
Astropy Collaboration, 2013, A&A, 558, A33
Astropy Collaboration, 2018, AJ, 156, 123
Astropy Collaboration, 2022, ApJ, 935, 167
Baraffe I., Chabrier G., 2018, A&A, 619, A177
Barclay T., Kostov V. B., Colón K. D., Quintana E. V., Schlieder J. E., Louie D. R., Gilbert E. A., Mullally S. E., 2021, AJ, 162, 300
Benneke B. et al., 2019, ApJ, 887, L14
Berdyugina S. V., 2009, in Strassmeier K. G., Kosovichev A. G., Beckman J. E., eds, Proc. IAU Symp. 259, Cosmic Magnetic Fields: From Planets, to Stars and Galaxies. Cambridge Univ. Press, Cambridge, p. 323
Briggs D. S., 1995, Bull. Am. Astron. Soc., 187, 1444
Browning M. K., 2008, ApJ, 676, 1262
Burgasser A. J., Putman M. E., 2005, ApJ, 626, 486
Burkhart B., Loeb A., 2017, ApJ, 849, L10
Callingham J. R. et al., 2021, Nat. Astron., 5, 1233
Callingham J. R. et al., 2024, Nat. Astron., 8, 1359
Caramazza M., Stelzer B., Magaudda E., Raetz S., Güdel M., Orlando S., Poppenhäger K., 2023, A&A, 676, A14
CASA Team et al., 2022, PASP, 134, 114501
Chabrier G., Küker M., 2006, A&A, 446, 1027
Charbonneau P., 2010, Living Rev. Sol. Phys., 7, 3
Charnay B., Blain D., Bézard B., Leconte J., Turbet M., Falco A., 2021, A&A, 646, A171
Climent J. B., Guirado J. C., Pérez-Torres M., Marcaide J. M., Peña-Moñino L., 2023, Science, 381, 1120
Cloutier R. et al., 2017, A&A, 608, A35
Dobler W., Stix M., Brandenburg A., 2006, ApJ, 638, 336
dos Santos L. A. et al., 2020, A&A, 634, L4
Driessen L. N., Williams D. R. A., McDonald I., Stappers B. W., Buckley D. A. H., Fender R. P., Woudt P. A., 2022, MNRAS, 510, 1083
Dulk G. A., 1985, ARA&A, 23, 169
Dulk G. A., Melrose D. B., White S. M., 1979, ApJ, 234, 1137
Farrell W. M., Desch M. D., Zarka P., 1999, J. Geophys. Res., 104, 14025
France K. et al., 2013, ApJ, 763, 149
Gloudemans A. J. et al., 2023, A&A, 678, A161
Golay W. W., Mutel R. L., Lipman D., Güdel M., 2023, MNRAS, 522, 1394
Güdel M., 2002, ARA&A, 40, 217
Güdel M., Benz A. O., 1993, ApJ, 405, L63
Guinan E. F., Engle S. G., 2019, Res. Notes Am. Astron. Soc., 3, 189
Günther M. N. et al., 2020, AJ, 159, 60
Henry T. J., Jao W.-C., Subasavage J. P., Beaulieu T. D., Ianna P. A., Costa E., Méndez R. A., 2006, AJ, 132, 2360
Henry T. J., Jao W.-C., 2024. Annual Review of Astronomy and Astrophysics, 62, 593
Kaltenegger L., Segura A., Mohanty S., 2011, ApJ, 733, 35
Kao M. M., Mioduszewski A. J., Villadsen J., Shkolnik E. L., 2023, Nature, 619, 272
Kellermann K. I., Pauliny-Toth I. I. K., 1969, ApJ, 155, L71
Lazio T. J. W., Farrell W. M., Dietrick J., Greenlees E., Hogan E., Jones C., Hennig L. A., 2004, ApJ, 612, 511
Lindegren L. et al., 2021, A&A, 649, A2
Madhusudhan N., Constantinou S., Holmberg M., Sarkar S., Piette A. A. A., Moses J. I., 2025, ApJ, 983, L40
Madhusudhan N., Piette A. A. A., Constantinou S., 2021, ApJ, 918, 1
Madhusudhan N., Sarkar S., Constantinou S., Holmberg M., Piette A. A. A., Moses J. I., 2023, ApJ, 956, L13
Mathys G., Solanki S. K., Wickramasinghe D. T., eds, 2001, ASP Conf. Ser. Vol. 248, Magnetic Fields Across the Hertzsprung-Russell Diagram. Astron. Soc. Pac., San Francisco, p. 248
McMullin J. P., Waters B., Schiebel D., Young W., Golap K., 2007, in Shaw R. A., Hill F., Bell D. J., eds, ASP Conf. Ser. Vol. 376, Astronomical Data Analysis Software and Systems XVI. Astron. Soc. Pac., San Francisco, p. 127
Melrose D. B., 1980, Space Sci. Rev., 26, 3
Melrose D. B., 2017, Rev. Mod. Plasma Phys., 1, 5
Modi A., Estrela R., Valio A., 2023, MNRAS, 525, 5168
Montet B. T. et al., 2015, ApJ, 809, 25
Nicholls H., Hébrard E., Venot O., Drummond B., Evans E., 2023, MNRAS, 523, 5681
O'Gorman E., Coughlan C. P., Vlemmings W., Varenius E., Sirothia S., Ray T. P., Olofsson H., 2018, A&A, 612, A52
Offringa A. R. et al., 2014, MNRAS, 444, 606
Parker E. N., 1955, ApJ, 122, 293
Pecaut M. J., Mamajek E. E., 2013, ApJS, 208, 9
Petrov L., Kovalev Y., 2025, ApJS, 276, 38
Pineda J. S., Villadsen J., 2023, Nat. Astron., 7, 569
Pohjolainen S., Talebpour Sheshvan N., 2020, Adv. Space Res., 65, 1663
Rau U., Cornwell T. J., 2011, A&A, 532, A71
Reid H. A. S., Kontar E. P., 2017, A&A, 598, A44
Reiners A., Schüssler M., Passegger V. M., 2014, ApJ, 794, 144
Rukdee S. et al., 2025, preprint (arXiv:2510.06939)
Sarkis P. et al., 2018, AJ, 155, 257
Schweitzer A. et al., 2019, A&A, 625, A68
Shields A. L., Ballard S., Johnson J. A., 2016, Phys. Rep., 663, 1
Shulyak D. et al., 2019, A&A, 626, A86
Smirnov O. M. et al., 2025, MNRAS, 538, L89
Tremblay C. D. et al., 2024, AJ, 167, 35
Venot O., Rocchetto M., Carl S., Roshni Hashim A., Decin L., 2016, ApJ, 830, 77
Villadsen J., Hallinan G., 2019, ApJ, 871, 214
Wandia K. et al., 2025, MNRAS, 543, 1935
Winters J. G. et al., 2019, AJ, 157, 216
Wu C. S., Lee L. C., 1979, ApJ, 230, 621
Zarka P., Treumann R. A., Ryabov B. P., Ryabov V. B., 2001, Ap&SS, 277, 293

This paper has been typeset from a TEX/LATEX file prepared by the author.